Available online at www.sciencedirect.com

jmr&t Journal of Materials Research and Technology

journal homepage: www.elsevier.com/locate/jmrt

Original Article

Full-stage precipitation during aging of Cu-0.55Cr-0.07Zr alloy for high heat flux fusion reactor technology

J. Hughes [a,*], T. Toyama [b], M. Gorley [c], E. Jimenez-Melero [a,**]

[a] Materials Performance Centre, Dept. of Materials, The University of Manchester, Manchester M13 9PL, UK
[b] Institute for Materials Research, Tohoku University, Oarai, Ibaraki 311-1313, Japan
[c] UK Atomic Energy Authority, Culham Science Centre, Abingdon, Oxfordshire, OX14 3DB, UK

ARTICLE INFO

Article history:
Received 25 April 2022
Accepted 17 July 2022
Available online 1 August 2022

Keywords:
Cu-base alloys
heat treatment
precipitation
microstructure characterization
fusion reactor technology

ABSTRACT

We have monitored the full-stage precipitate evolution in Cu-0.55Cr-0.07Zr alloy during aging at 480 °C (753 K) up to 14 days (20160 min), using micro-hardness, positron annihilation spectroscopy, electron microscopy and atom probe tomography. Cr-rich precipitates form during the early stages of aging, and after 5.5 min the distribution is characterised by a number density of 8×10^{23} m^{-3} and an average precipitate size of 2.5 nm. At that time, Zr segregation is also detected at the precipitate sites. Longer aging times lead to precipitate coarsening, simultaneously with the occurrence of a Zr-rich shell around precipitates potentially to help reduce local coherency strains. Peak aging of the alloy is attained after 120 min of aging, and overaging induces further precipitate coarsening and the transition from spherical to disc-like morphology. At the longest aging time of 14 days, the precipitates maintain a face-centred cubic symmetry, reaching an average size of ~9 nm at a density of 0.2×10^{22} m^{-3}. The presence of Zr atoms at the precipitate site and interface, and the disc-like morphology of overaged precipitates, should be considered when assessing the precipitate stability under irradiation and the precipitate/matrix interface as a potential sink for radiation-induced lattice defects.

1. Introduction

Precipitation-hardened CuCrZr alloy is selected for the manufacture of high heat flux components in the divertor and first wall of magnetically-confined fusion tokamaks [1-5]. The compositional ranges of the CuCrZr alloy, as specified in the European standards EN 12167:1998 and EN 12165:1998, are 0.5-1.2 wt.% Cr and 0.05-0.25 wt.% Zr [6]. The mechanical strength - thermal conductivity balance of the material is modified by an initial solution annealing for 0.5-2 h at 980-1000 °C (1253-1273K), followed by water quenching and aging for 2-4 h at 450-480 °C (723-753 K), aiming to form a homogeneous dispersion of Cr-rich precipitates of ~2-3 nm in diameter

* Corresponding author.
** Corresponding author.
E-mail addresses: jonathanhughes@studygroup.com (J. Hughes), enrique.jimenez-melero@manchester.ac.uk (E. Jimenez-Melero).
https://doi.org/10.1016/j.jmrt.2022.07.113

within the Cu-base matrix close to peak aging condition [4, 6]. However, additional brazing and diffusion bonding processes at temperatures > 480°C (>753 K) can induce overaging and coarsening of the precipitate distribution, having a detrimental effect on the mechanics of the material [6, 7].

The high density of Cr precipitates and their interfaces with the Cu matrix possess enhanced sink strength levels for the recombination of vacancies and self-interstitials generated by neutron bombardment [1]. Therefore, those precipitates provide the material with high tolerance to radiation-induced degradation phenomena such as void swelling [1, 4]. Unfortunately, specimens irradiated at temperatures < 200 °C undergo strain localization along channels of ~100-250 nm thick that are generally clear of shearable precipitates, dislocations and other lattice defects, resulting in severe loss of work hardening capability and uniform elongation [6-8]. Moreover, with irradiation at temperatures > 300 °C (> 573 K) the alloy experiences softening and thermal creep effects associated with the recovery of dislocation structures and the simultaneous coarsening of those Cr-rich precipitates [4, 6].

The nano-scale Cr precipitation during material's processing has been reported in a range of dilute Cu-Cr model alloys. Aging at 450 °C triggers the appearance of Cr-rich Guinier-Preston (GP) zones and coherent matrix strains, that give rise to metastable face-centred-cubic (fcc) spherical precipitates and enhanced lattice strains along the <110> direction of the Cu matrix [9]. The precipitate evolution with time into an ordered fcc phase, possessing a cube-on-cube orientation relationship with the matrix, seems to act as an intermediate stage in the formation of larger incoherent body-centred-cubic (bcc) precipitates [9, 10]. There is a coexistence of fcc & bcc precipitates at aging times of 1-24 h, whereas the binary Cu-Cr alloy reaches peak strength after 8 h of aging [9]. Extended aging times lead to bcc precipitate coarsening, and to the predominance of the Kurdjumov-Sachs over the Nishiyama-Wassermann orientation relationship [11].

The presence of Zr in solid solution in the Cu matrix facilitates the formation of a homogeneous Cr-rich precipitate distribution [12]. Zr also reduces the stacking fault energy of the matrix, and therefore increases the propensity for twin formation and the fatigue resistance of the alloy [13]. However, it simultaneously facilitates the generation of dissociated dislocations and stacking fault tetrahedra in radiation environments. The role and impact of Zr on the sequence of Cr-rich precipitation during aging remain unconfirmed. Limited electron diffraction results suggest that Zr might promote the formation of an ordered B2 (CsCl-type) structure from the ordered fcc phase, potentially evolving at longer times into the bcc precipitates [14]. In binary Cu-Zr alloys, aging leads to the formation of Zr clusters composed of disc-shaped monolayers of Zr atoms that evolve into semi-coherent, disc-like Cu_5Zr precipitates, and therefore limits the Zr amount in solid solution in the Cu matrix [15]. Moreover, in the Cu-rich region of the Cu-Zr phase diagram, Cu_5Zr undergoes a eutectoid decomposition reaction into fcc-Cu + $Cu_{51}Zr_{14}$-β [16]. Other Cu-Zr precipitate stoichiometries have also been reported in the literature ([15, 16]). Overaging for 1 h at 600 °C (873 K) of Cu-Cr-Zr specimens initially in the peak aged condition is reported to cause the formation of a Cu_7Cr_3ZrSi shell surrounding the Cr-rich spherical precipitates. An additional 3 h of overaging at 600 °C (873 K) promotes the thick-plate morphology of the precipitates during growth [17, 18].

In this work, we have monitored the time-dependent precipitate sequence and associated changes in local microchemistry in Cu-Cr-Zr alloy during the thermal aging treatment at 480 °C (753 K) up to 14 days (20160 min), after solution annealing, to pinpoint the Zr role during the early stages of precipitation and the subsequent longer overaging behaviour of the precipitates. This systematic material processing study is in support of current material property database & handbook campaigns to inform, for instance, EU-DEMO design selections, since material properties are found to be very sensitive to heat treatment parameters, as compared to other parameters such as the alloy chemistry or test specimen size [19].

2. Experimental

The chemical composition of the as-received bar material, as determined by inductively coupled plasma mass spectrometry, is given in Table 1. Equivalent samples with a cross section of 10×10 mm^2 and ~1 mm thick were cut from the initial CuCrZr material, solutioned annealed in inert atmosphere at 1000 °C (1273 K) for 2 h, and subsequently water quenched to maintain the supersaturated solid solution of Cr and Zr in Cu. Afterwards, the samples were aged in inert atmosphere at 480 °C (753 K), each at a selected aging time up to 14 days (20160 min), and finally water quenched to room temperature. The Vickers micro-hardness of the annealed samples was measured using a load of 1.0 kgf and a duration of 10 s. Mean values for each sample were calculated from 10 micro-hardness measurements. We have undertaken a final water quenching step to room temperature to avoid any potential microstructural changes during cooling from the aging temperature. This approach was adopted for all aging times for consistency, and to follow the recommended practice in the nuclear fusion community to avoid a reduction in peak hardness and mechanical properties expected in case of furnace or air cooling [37]. However, water quenching would not be strictly necessary in the case of 14 days of aging at 480 °C, since the microstructure is overaged prior to the final cooling to room temperature, as discussed later in section 3.

For scanning electron microscopy (SEM) after aging, specimens after heat treatment were prepared by mechanical

Table 1 – Chemical composition (wt.%) of the Cu-Cr-Zr alloy used in this study, determined by inductively coupled plasma mass spectrometry.

Cr	Zr	Zn	Fe	Si	Sn	Pb	Al	Ni	Cu
0.550	0.074	0.038	0.025	0.009	0.002	<0.001	<0.003	<0.001	Bal.

grinding to 4000 grit SiC paper, followed by electro-polishing using an electrolyte of 10 vol.% nitric acid and 90 vol.% methanol at the temperature of -40 °C (233 K). High-resolution backscattered electron (BSE) imaging was carried out on an FEI Magellan HR FEG-SEM microscope equipped with a concentric backscattered (CBS) detector [20, 21]. The average grain size in the Cu matrix was calculated using the linear intercept method from BSE micrographs. EBSD maps of the same region of interest as for the BSE analysis, and EDS maps in selected regions containing inclusions, were collected using an Oxford Instrument Electron Backscattered Diffraction (EBSD) detector and an Energy-dispersive X-ray Spectroscopy (EDS) detector, respectively, both also available on the same FEI Magellan microscope. The EBSD and EDS data processing was performed using the Aztec software from Oxford Instruments. In the EBSD data analysis, low-angle grain boundaries (LAGB) were classified as presenting a misorientation angle between 2° and 15° and high-angle grain boundaries (HAGB) as those with an angle >15° [22, 23].

For transmission electron microscopy (TEM) imaging and analysis, 3mm-diameter discs were prepared by mechanical pre-thinning, followed by electro-polishing using the same electrolyte and temperature as previously mentioned. TEM characterization of the precipitate distribution was performed using an FEI Tecnai G2 20 microscope with a LaB_6 source and an accelerating voltage 200 kV, whereas the chemical analysis of the precipitates was based on STEM-EDX measurements using an FEI Talos F200A microscope. The analysis of the EDX spectra was performed using the FEI Velox analysis software. The average diameter of the nano-sized precipitates was measured using Cr $K\alpha$ elemental maps. In case of disc-shaped precipitates, the diameter corresponds to the average value of the short and long distance. The foil thickness was derived from the fringes spacing in convergent beam electron diffraction patterns (CBED) [24]. The foil thickness values obtained were ~40-50 nm. Additionally, 3D-atom probe (3D-AP) tomography measurements were taken of samples in the solution annealed, and in aging condition after 5, 60 and 1440 min at 480 °C. Needle-like samples for 3D-AP analysis were prepared via a micro-sampling method using a focused ion beam [25]. 3D-AP maps were collected using a laser-assisted local-electrode type atom probe by IMAGO Scientific Instruments, LEAP-3000XHR, at an evaporation rate of 0.4 per laser pulse, applying a laser power of 20 nJ, a laser pulse repetition rate of 200 kHz, a DC voltage in the range from 3 to 8 kV, and a base specimen temperature of -238 °C (35 K). Laser pulse mode was used during the 3D-AP measurements due to the high probability of fracture for these samples in voltage pulse mode. To reduce the probability of fracture, we employed laser pulse mode in relatively high power (20 nJ). The 3D-AP datasets were analysed using the dedicated software IVAS 3.6.4 from IMAGO Scientific Instruments.

Local microstructural changes during aging were also assessed using Positron Annihilation Spectroscopy (PAS) [26, 27]. A ~1 MBq Na-22 positron source, sealed in Kapton foil, was placed between two equivalent CuCrZr samples of ~1 mm in thickness. The positron lifetime spectra were acquired using a fast-fast BaF_2 spectrometer with time resolution ~180 ps at full width half maximum. The data were corrected for the background and source contributions, and they were analysed using the PALSfit software package [28]. Each recorded spectrum comprised ~4×10^6 coincidence events. Two high-resolution Ge detectors set up in coincidence were also used to record simultaneously the coincidence Doppler broadening (CDB) spectra of the annihilation radiation. Positron-electron annihilation releases two γ-ray photons at 180° to each other. The total energy of the electron-positron pair at the point of the annihilation event (E_T) is the sum of the energies of these two γ-rays. Therefore $E_T = E_1 + E_2 = 2m_0c^2 - E_B$ where E_1 and E_2 are the energies of the two γ-rays, m_0 is the rest mass of an electron or positron, c is the speed of light, and E_B is the electron-positron binding energy. It should be noted, however, that E_1 and E_2 are not equal depending on p_L, i.e. the longitudinal component of the momentum of the electron-positron pair in the direction of the γ-ray emission. $\Delta E = E_1 - E_2 = cp_L$ where ΔE is the difference in energy between the two emitted γ-rays [29]. From the measured CDB spectra, we derived the S- and W- line shape parameters at each probed aging time, by taking the ratio of the low momentum ($|p_L| < 4 \times 10^{-3}\, m_0c$) and high momentum ($10 \times 10^{-3}\, m_0c < |p_L| < 18 \times 10^{-3}\, m_0c$) region of the spectrum to the total region, respectively. The overall momentum resolution was ~$4\times10^{-3}\, m_0c$. We also measured the CDB spectrum of three reference polycrystalline samples: (i) a Cu sample (99.999%) annealed at 800 °C (1073 K) for 1 h in He gas atmosphere, (ii) a Cr sample (99.99%) annealed at 1100 °C for 1 h in vacuum, and (iii) a Zr sample (99.2%) annealed at 900 °C (1173 K) for 2 h in vacuum. The *S*-parameter represents lower-momentum valence electron annihilations with the implanted positrons, making it more responsive to the presence of low electron density areas in the material such as vacancies and voids. Conversely, the W-parameter reveals information about the positron annihilation with higher-momentum core electrons, and therefore reveals the local chemical environment of the positron site [26, 30].

3. Results

Fig. 1 shows the BSE micrographs of the Cu-Cr-Zr microstructure in the solution annealed (SA) state and at selected times during aging at 480 °C (753 K). The average grain size of the matrix remains constant within the standard deviation of the size distribution (~35 μm), with a value of ~ 36-38 μm throughout the aging process up to 14 days. The high standard deviation arises from the presence of larger grains (≥ 100 μm) in all the specimens. Grain boundary analysis from EBSD maps (Fig. S1) did not reveal any significant variation with aging, with all samples showing ~5% low angle grain boundaries, ~40% twins, and ~55% large angle boundaries. The solution annealed microstructure also contained relatively large (mostly Cr but also some Zr-rich, see EDS data in Fig. S2) inclusions that were already present in the as-received bar material.

The material's hardness remains relatively low and constant within the first 3 min of annealing at a value ~50 $HV_{1.0}$, but the hardness thereafter experiences a rapid increase after 5.5 min attaining a value of 95 $HV_{1.0}$ (see Fig. 2a). As aging progresses further, the hardness continues to increase and gradually levels off at ~135 $HV_{1.0}$ at the aging time of 120 min. At longer times there is a noticeable reduction in hardness to ~120 $HV_{1.0}$ measured after a full 24 h (i.e., 1440 min) of aging. The time dependence of the positron lifetime during aging is

shown in Fig. 2b. The lifetime in the solution annealed state amounts to 137 ps. There is a sharp increase in lifetime between 3.0 and 5.5 min, in line with the trend observed in the hardness' values, with the lifetime reaching a value of 150 ps. Thereafter the positron lifetime gradually decreases to 140 ps after 24 h of aging. The (S, W) values for the different aging times, together with the measured values for the annealed polycrystalline Cu, Cr and Zr materials as reference, are collected in Fig. 3. The datapoints for the first 3.0 min of aging are clustered together and lie close to the values for the annealed Cu sample. However, in the case of 5.5, 7.0 and 10 min, the S parameter is shifted to higher values, and the W parameter to lower values, both shifted towards the annealed Zr reference. At longer times, the (S, W) data points invert the trend and are shifted partially back towards the annealed Cr and esp. Cu reference values.

3D-AP data reveal the presence of a fine dispersion of Cr-rich spherical precipitates with a number density of $N = 8\times10^{23}$ m^{-3} and an average diameter of $d = 2.5$ nm after only 5.5 min of aging, whereas no such precipitate structure was observed in the solution annealed state (Fig. 4). There is also a non-negligible segregation of Zr atoms at the precipitate locations. The volume fraction (f) for spherical precipitates can be estimated according to [4]:

$$f = \frac{\pi N d^3}{6} \quad (1)$$

This yields a volume fraction of $f \sim 0.65$ vol.% after 5.5 min of aging. As aging progresses to 60 min, the precipitate distribution becomes better defined, with the precipitates having coarsened to 3.2 nm in average diameter and the number density having reduced to 2.64×10^{23} m^{-3}. In the sample aged for 1440 min (24 h), the precipitates have coarsened yet further to a mean diameter of 8.5 nm, with the lowest number density of 2.3×10^{22} m^{-3} and a volume fraction of $f \sim 0.73$ vol.%, and they have adopted a disc-shaped morphology primarily. The spherical morphology of the Cr-rich precipitates at aging times $\leq$ 60 min, and the presence of disc-like precipitates at longer times is also evidenced by the STEM-EDX data (Fig. 5). Furthermore, there is Zr segregation at the precipitate/matrix interface in disc-like precipitates after 1440 min (24 h) of aging, with an average Zr shell thickness of ~2 nm from EDX profiles, and the precipitates maintain a fcc structure, see Fig. 6.

4. Discussion

The microstructure in the solution annealed state comprises a fcc Cu-base matrix and Cr-rich inclusions (Fig. 1). The Cr solubility in Cu at 1000 °C (1273 K) amounts to ~0.37 wt.% [13]. Consequently, coarse Cr-rich precipitates from solidification remain undissolved in the Cu matrix after solution annealing [31], and they do not undergo changes during aging. The SA sample gives a relatively low hardness value of ~50 $HV_{1.0}$, and a positron lifetime of 137 ps (Fig. 2). The 3D-AP data have not shown the presence of nm-sized precipitates in the SA state (Fig. 4). Positrons are implanted into the Cu-Cr-Zr material,

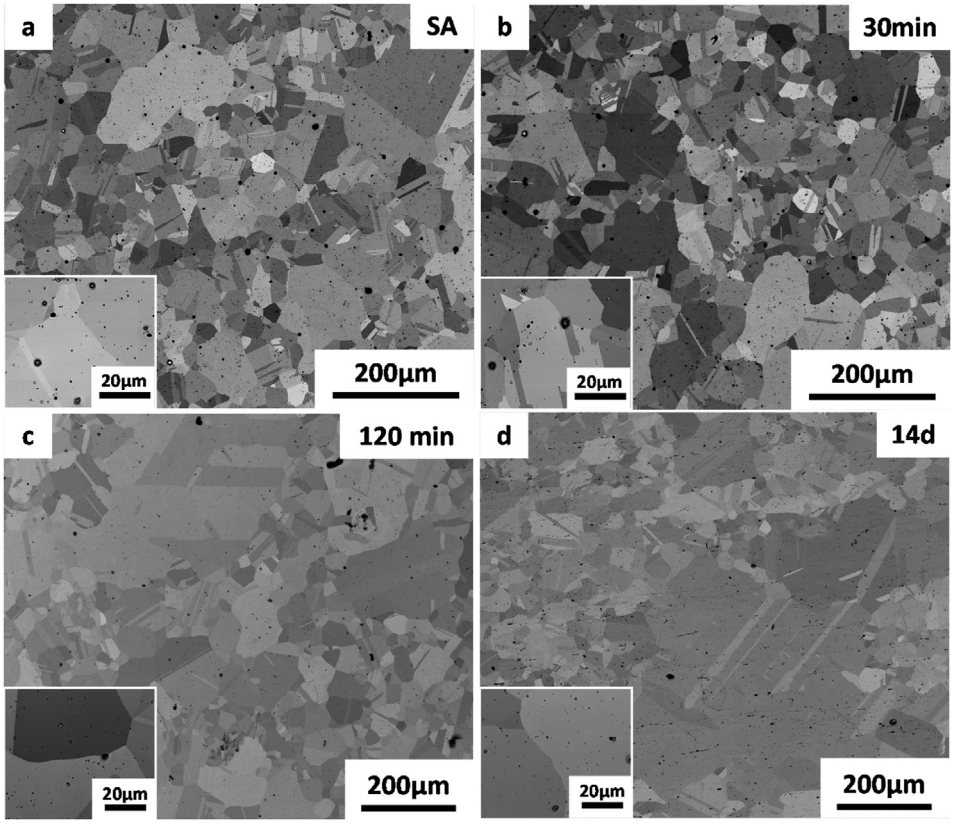

Fig. 1 – BSE micrographs of Cu-Cr-Zr alloy in (a) the solution annealed (SA) state, and aged at 480 °C (753 K) for (b) 30 min, (c) 2 h, and (d) 14 days.

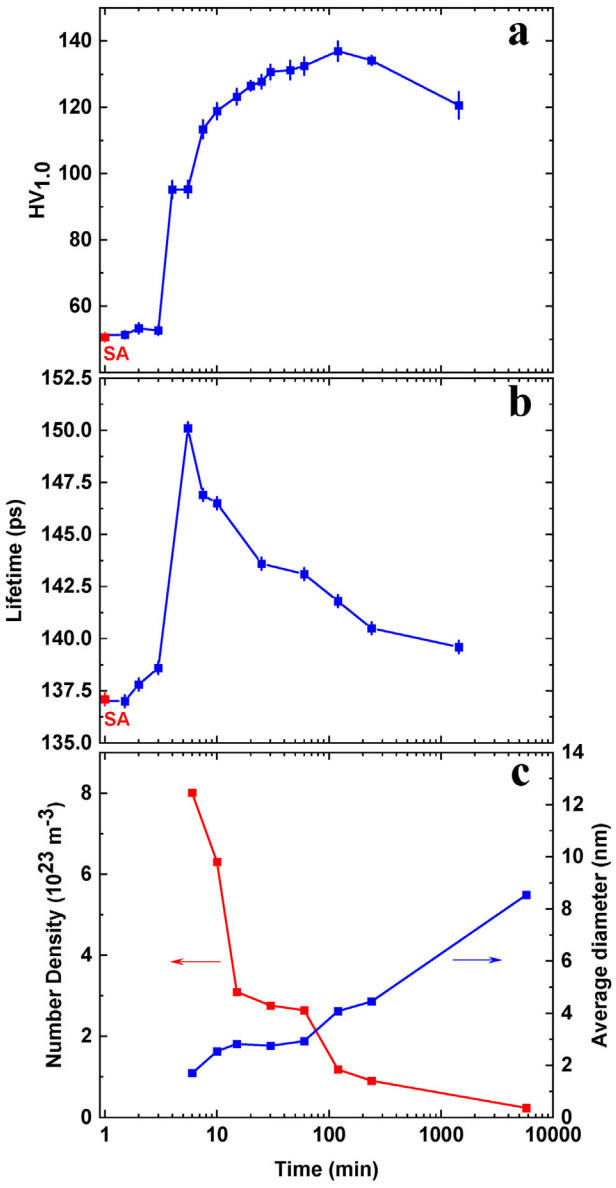

Fig. 2 – Time dependence at the aging temperature of 480 °C (753 K) of (a) the microhardness ($HV_{1.0}$), (b) the positron lifetime, and (c) the number density and average size of the precipitates in Cu-Cr-Zr alloy, obtained by 3D-AP and TEM characterisation. 'SA' denotes the solution-annealed state of the material.

where they thermalise and become trapped at preferred locations in the microstructure. Self-consistent electron structure and positron band structure calculations revealed a higher positron affinity for Cu as compared to Zr, and especially to Cr [32]. Therefore, the implanted positrons would in principle become annihilated preferentially within the Cu-base matrix. However, the value of 137 ps is higher than the reported positron lifetime in bulk Cu single crystal of 110 ps. Vacancies and other open-volume lattice defects such as dislocations or interfaces (e.g. precipitate/matrix interfaces) can also act as effective positron trapping sites, and increase the positron lifetime. Positrons have a lifetime of 173 ps in monovacancy defects and 163 ps when trapped in dislocations in Cu [18]. We have only detected one component in the positron lifetime spectra in all measured samples. Such component represents the average lifetime in bulk Cu single crystal and in open volume defects.

During the first 3 min of aging at 480 °C (753 K), there is a subtle increase in hardness and also in the positron lifetime, signalling the onset of Cr-rich precipitate formation. In contrast, when the aging time increases to 5.5 min we detected a sharp increase in both the material's hardness and the positron lifetime. At this time Cr-rich spherical precipitates are clearly observed in the microstructure (Fig. 4 and 5), with a number density of 8×10^{23} m^{-3} and an average precipitate size of 2.5 nm. The Cr diffusion coefficient in Cu depends on temperature, in the range of 366 to 556 °C (639 to 839 K), according to [33]:

$$D_{Cr} = 0.26 \times 10^{-4} \times exp\left(\frac{-1.99\ eV}{k_B T}\right) \quad (2)$$

where k_B denotes the Boltzmann constant at T the temperature in K. At the aging temperature of 480 °C (753 K), the Cr diffusion coefficient amounts to $D_{Cr} \approx 1.25 \times 10^{-18} m^2 s^{-1}$. If we assume a random walk for the Cr diffusion in Cu, we obtain a Cr diffusion length of $\sqrt{Dt} \approx 20\ nm$ after 5.5 min of aging. Furthermore, the 3D-AP data also revealed the presence of Zr atoms in the same locations as the Cr-rich precipitates (Fig. 4). The increase in hardness and positron lifetime, and the presence of precipitates, is supported by the trend observed in the (S, W) values as a function of aging time (Fig. 3). A linear trajectory in the S-W plot is normally associated with changes in the fraction of positron annihilations at competing sites presenting different open space and local chemical environment for the implanted positrons [34]. The (S, W) values for aging times $\leq$ 3.0 min lie in close vicinity to the values for annealed Cu, whereas the data points for 5.5 to 10 min are shifted to higher values of the S parameter, reflecting a higher amount of open-volume defects close to the precipitate/matrix interface. There is also a reduction in the W parameter as

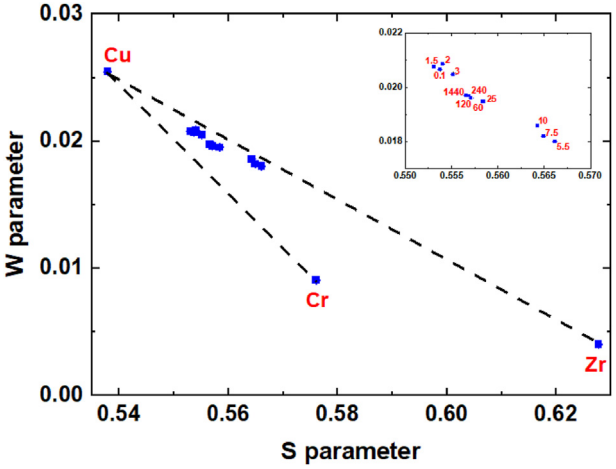

Fig. 3 – S-W parameter plot for Cu-Cr-Zr samples aged at 480 °C (753 K) after solution annealing. The aging time is labelled close to each data point. The plot also contains the experimental S-W values of the annealed Cu, Cr and Zr samples as reference.

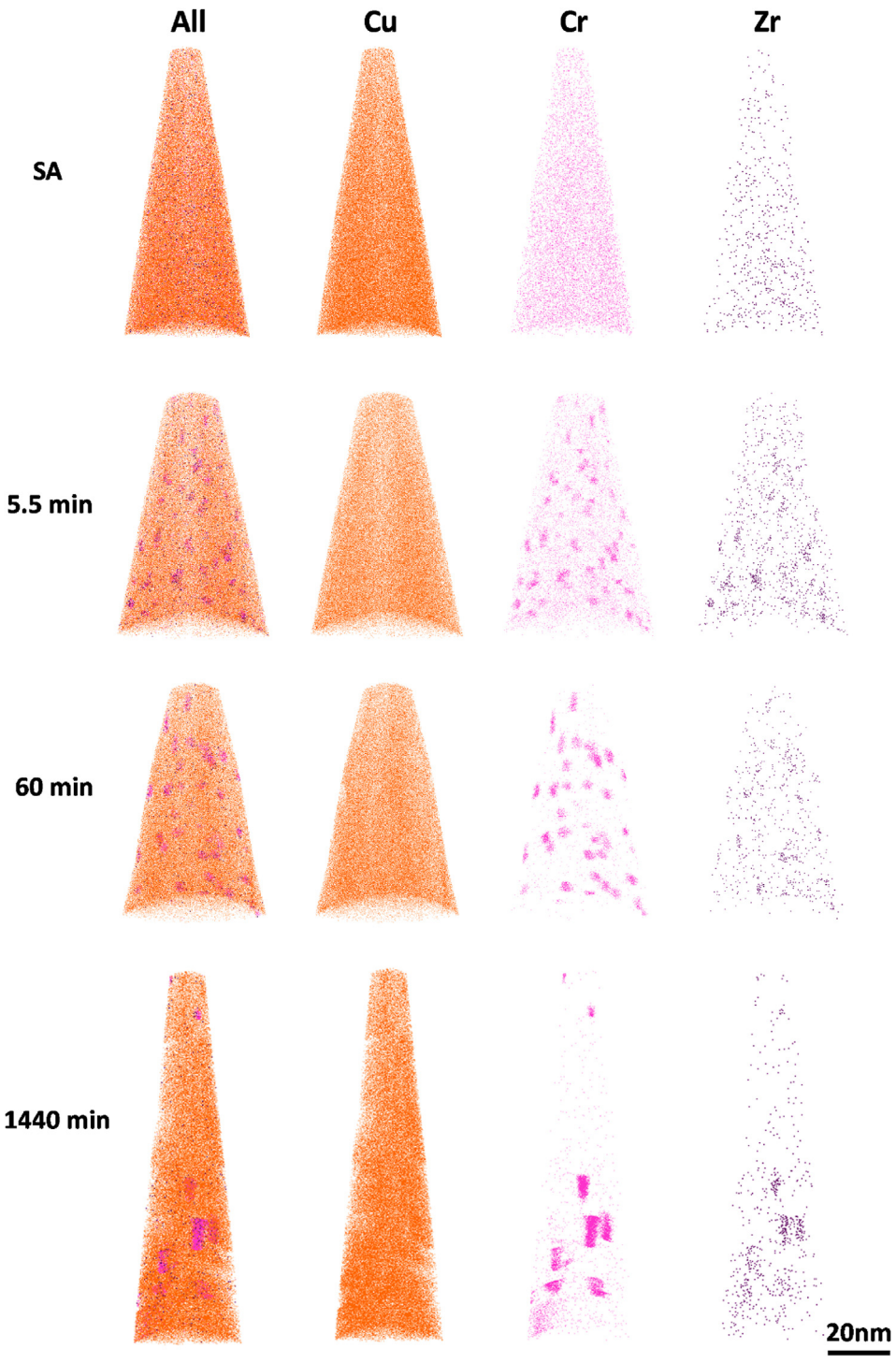

Fig. 4 – 3-D atom probe tomography (APT) data revealing the evolution of Cr-rich precipitates after aging the Cu-Cr-Zr alloy at 480 °C (753 K) for 5.5, 60 and 1440 min, together with the APT data for the solution annealed (SA) state as reference.

compared to shorter times, and in line with the value for annealed Zr. The shift observed in the (S, W) plot implies a higher fraction of positrons trapped at the precipitate/matrix interface, where Zr atoms are present in the precipitates close to that interface. In this case, the increase in positron lifetime at the aging time of 5.5 min, as compared to the solution annealed condition, can consistently be ascribed to the Zr content in the Cr-rich precipitates, since the positron lifetime in bulk Zr equals to 168.5 ps, whereas the lifetime increases to 253.7 ps in Zr monovacancies and to 217 ps in dislocations in Zr [35]. Those values are higher than the corresponding positron lifetime in bulk Cu of 110 ps and in Cu monovacancies of 173 ps [18], but also than in bulk Cr of 108 ps and in Cr monovacancies of 198 ps [36].

At aging times longer than 5.5 min, the material's hardness increases with time at a lower rate, attaining peak aging at 120

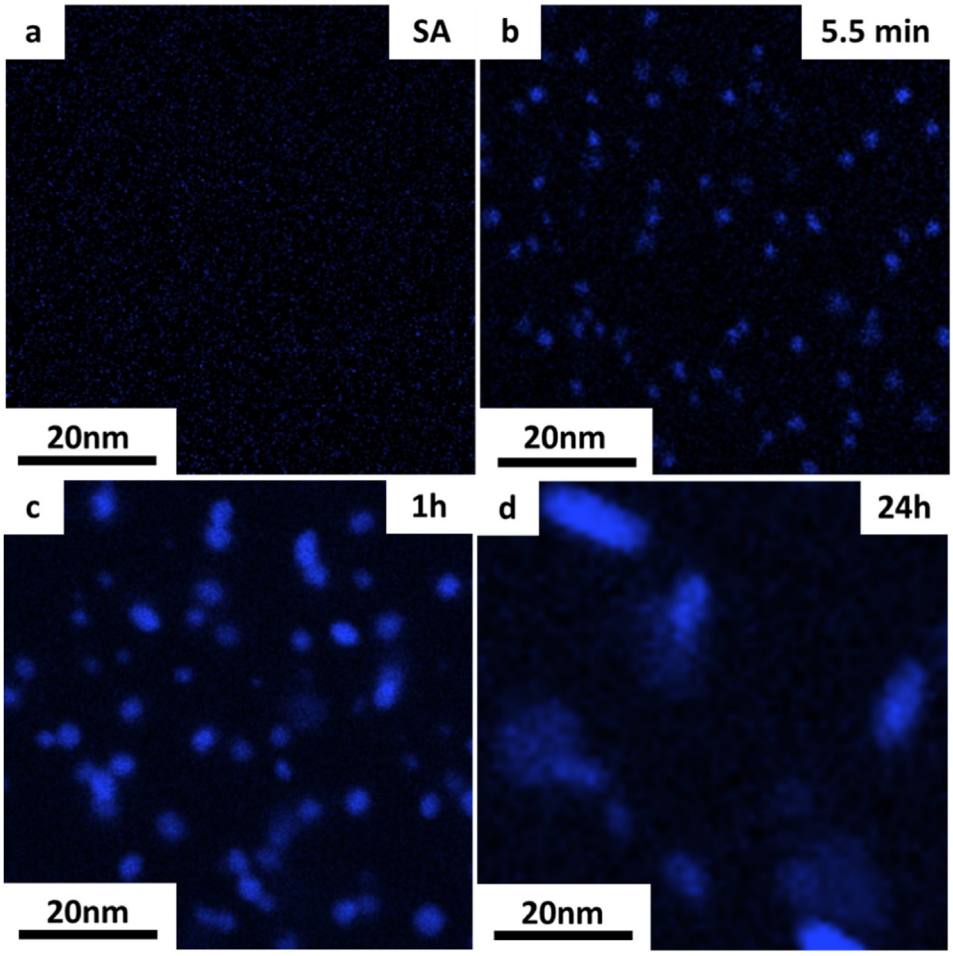

Fig. 5 – Cr Kα elemental maps showing the evolution Cr-rich precipitates at selected states during the aging of CuCrZr alloy at 480 °C (753 K), namely in the (a) solution annealed condition, and after (b) 5.5 min, (c) 1 h, and (d) 24 h.

min, and thereafter undergoing a gradual reduction in hardness during overaging (Fig. 2a). Overaged Cu-Cr-Zr microstructures are characterised by reduced values of yield and tensile strength in tensile specimens [7, 37-41], although overaging can provide the alloy with limited gains in resistance to plastic instability and in fracture toughness after neutron irradiation [7]. Semi-coherent Cr-rich precipitates were observed by in-situ TEM to act as effective pinning sites for dislocation gliding, with dislocations disengaging from the precipitates predominantly by a shear mechanism [42]. The peak aged condition also corresponds to an enhanced conductivity in the alloy [38]. The Zr remaining in solid solution in the Cu matrix can further increase the alloy strength at peak aging [39].

The nano-sized precipitate distribution experiences a continuous coarsening during aging at 480 °C, with a reduction in number density and an increase in average precipitate size to values of 0.2×10^{22} m^{-3} and ~9 nm respectively at the longest aging time of 14 days (Fig. 2c). The precipitate coarsening causes a reduction in precipitate/matrix interfacial area and consequently also in the positron lifetime (Fig. 2b). Moreover, the (S, W) plot in Fig. 4 shows a partial shift backwards of the data points corresponding to aging times > 5.5 min to initial values and closer to those of annealed Cu and Cr, reflecting a reduction in Zr presence in the positron sites at the precipitate/matrix interface as the precipitates coarsen. At the aging time of 60 min the precipitates present a preferential spherical morphology. However, at the longer time of 1440 min, past the peak aging condition of the material, there is a mixture of spherical and disc-like precipitates, with a Zr shell being detected at the interface in disc-like precipitates. Previous results suggested the need to overage the peak aged microstructure of Cu-078Cr-0.13Zr alloy at 600 °C (873 K) for at least 1 h to observe the formation of a Zr shell surrounding the nano-sized precipitates [18]. Zr segregation at the periphery of metastable fcc Cr-rich precipitates has also been reported in a quaternary Cu-Cr-Zr-Ti alloys [43]. The electron diffraction data in this work shows that the precipitates in Cu-0.55Cr-0.07Zr alloy remain with fcc symmetry beyond the peak aging time in this alloy of 120 min. A higher amount of Zr addition to a Cu-0.8Cr alloy, namely 0.2 wt.% Zr, induces the formation of ordered fcc Cr-rich precipitates with ellipsoid-shaped morphology at peak aging time at 450 °C [44]. This is in contrast with the reported results in the literature in binary Cu-Cr alloys, where the peak aging occurs at a longer aging time of 8 h, with a mixture of fcc and bcc precipitates being observed at precipitates sizes smaller than 10 nm [9].

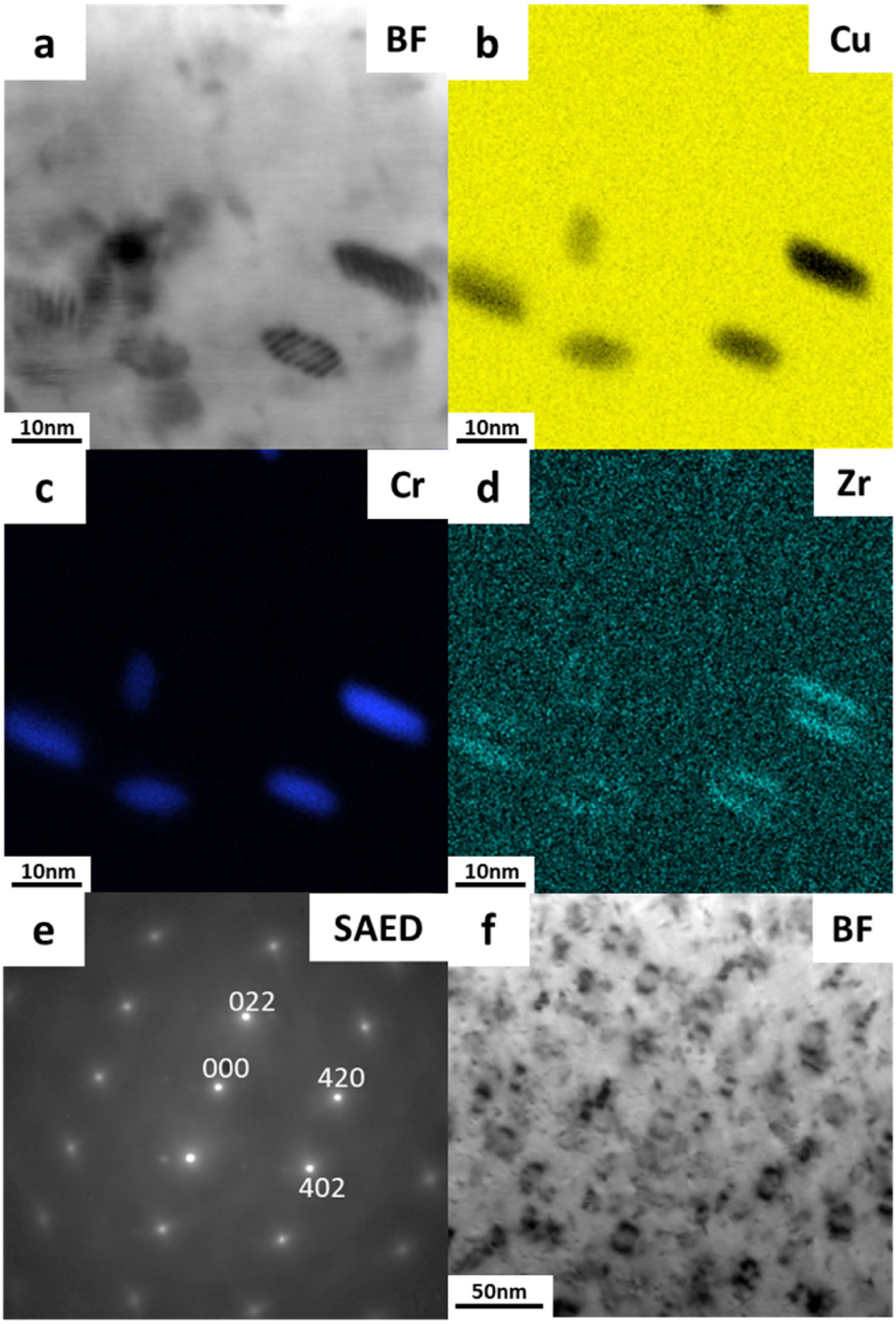

Fig. 6 – STEM-EDX maps taken from CuCrZr after 24 h aging at 480 °C (753 K) showing (a) bright field STEM, (b) Cu, (c) Cr, and (d) Zr elemental maps, (e) a selected area diffraction pattern demonstrating the {-122} zone axis, and (f) BF STEM image of selected precipitates.

The incorporation of 0.07 wt.% Zr in the alloy seems to lead to a shorter peak aging time, but also to the stabilization of the fcc symmetry at longer times and potentially affecting the final morphology of the precipitates post-aging.

Aging at 480 °C is recommended since it yields the highest hardness and tensile strength in the peak aged condition in this precipitation-hardened alloy [6]. Similar (over-)aging behaviour of the Cr-rich precipitate distribution is expected to occur at shorter times when using aging temperatures higher than 480 °C. In practice, local temperatures may be higher than 480 °C, e.g. during joining of materials. This can cause overaging of the microstructure and lower tensile strength levels, although still higher than in pure Cu and within the accepted range for high-flux structural components [6]. Additionally, an overaging treatment could for instance be adopted at 600 °C for 1 h to increase the alloy ductility and

fracture toughness [7], esp. after neutron irradiation, although at the expense of a reduction in tensile strength.

5. Conclusions

We have probed the nm-sized precipitate evolution during aging at 480 °C (753 K) of a solution annealed Cu-Cr-Zr alloy. Spherical Cr-rich precipitates form during the early stages of aging, reaching an average size of 2.5 nm and a number density of 8×10^{23} m^{-3} after 5.5 min. At that time, we also detected the presence of Zr segregation at the precipitate locations. As the aging progresses further, the precipitates coarsen as the number density decreases. At 60 min of aging, we detected the presence of a Zr-rich shell around Cr-rich precipitates. The peak aging corresponds to 120 min at that temperature, significantly shorter than the reported time at maximum hardness in binary Cu-Cr alloys. Overaging causes further precipitate coarsening to an average size of ~9 nm at a density of 0.2×10^{22} m^{-3}, while maintaining the face-centre cubic symmetry and evolving into a disc-like morphology. These results point at the Zr role in stabilising the intermediate fcc structure and potentially affecting the overaged precipitate morphology.

Declaration of Competing Interest

The authors declare that they have no known competing financial interests or personal relationships that could have appeared to influence the work reported in this paper.

Acknowledgments

The authors of this work acknowledge the support of Culham Centre for Fusion Energy (CCFE). Mike Gorley would like to acknowledge funding from the EPSRC Grant EP/T012250/1. We also thank the International Research Centre for Nuclear Materials Science of the Institute for Materials Research, Tohoku University, for their financial travel support, as well as access to equipment and assistance in carrying out PAS and 3D-AP experiments.

Appendix A. Supplementary data

Supplementary data to this article can be found online at https://doi.org/10.1016/j.jmrt.2022.07.113.

REFERENCES

[1] Fabritsiev SA, Zinkle SJ, Singh BN. Evaluation of copper alloys for fusion reactor divertor and first wall components. J. Nucl. Mater. 1996;233-237:127–37.
[2] Tanaka S, Matera R, Kalinin G, Barabash V, Mohri K. ITER Materials R&D Data Bank. J. Nucl. Mater. 1999;271&272:478–85.
[3] Hirai T, Ezato K, Majerus P. ITER Relevant High Heat Flux Testing on Plasma Facing Surfaces. Mater. Trans. 2005;46:412–24.
[4] Zinkle SJ. Applicability of copper alloys for DEMO high heat flux components. Phys. Scr. 2016;T167:14004.
[5] Hirai T, Barabash V, Escourbiac F, Durocher A, Ferrand L, Komarov V, Merola M. ITER divertor materials and manufacturing challenges. Fusion Eng. Des. 2017;125:250–5.
[6] Barabash VR, Kalinin GM, Fabritsiev SA, Zinkle SJ. Specification of CuCrZr alloy properties after various thermo-mechanical treatments and design allowables including neutron irradiation effects. J. Nucl. Mater. 2011;417:904–7.
[7] Edwards DJ, Singh BN, Tähtinen S. Effect of heat treatments on precipitate microstructure and mechanical properties of a CuCrZr alloy. J. Nucl. Mater. 2007;367-370:904–9.
[8] Li M, Zinkle SJ. Physical and Mechanical Properties of Copper and Copper Alloys. In: Comprehensive Nuclear Materials, vol. 4. Elsevier; 2012. p. 667–90.
[9] Peng L, Xie H, Huang G, Xu G, Yin X, Feng X, Mi X, Yang Z. The phase transformation and strengthening of a Cu-0.71 wt% Cr alloy. J. Alloys Comp. 2017;708:1096–102.
[10] A. Chbihi, X. Sauvage, D. Blavette, Atomic scale investigation of Cr precipitation in copper, Acta Mater. 60 (1012) 4575-4585.
[11] Fujii T, Nakazawa H, Kato M, Dahmen U. Crystallography and morphology of nanosized Cr particles in a Cu-0.2% Cr alloy. Acta Mater 2000;48:1033–45.
[12] Kalinin G, Barabash V, Cardella A, Dietz J, Ioki K, Matera R, et al. Assessment and selection of materials for ITER in-vessel components. J. Nucl. Mater. 2000;283±287:10–9.
[13] Batra IS, Dey GK, Kulkarni UD, Banerjee S. Microstructure and properties of a Cu-Cr-Zr alloy. J. Nucl. Mater. 2001;299:91–100.
[14] Batra IS, Dey GK, Kulkarni UD, Banerjee S. Precipitation in a Cu-Cr-Zr alloy. Mater. Sci. Eng. A 2002;356:32–6.
[15] Peng L, Xie H, Huang G, Li Y, Yin X, Feng X, Mi X, Yang Z. The phase transformation and its effects on properties of a Cu-0.12 wt% Zr alloy. Mater. Sci. Eng. A 2015;633:28–34.
[16] Zhou SH, Napolitano RE. Phase stability for the Cu–Zr system: First-principles, experiments and solution-based modelling. Acta Mater 2000;58(6):2186–96.
[17] Hatakeyama M, Tokama T, Nagai Y, Hasegawa M, Eldrup M, Singh BN. Nanostructural Evolution of Cr-rich Precipitates in a Cu-Cr-Zr Alloy During Heat Treatment Studied by 3-Dimensional Atom probe. Mater. Trans. 2008;49:518–21.
[18] Hatakeyama M, Toyama T, Yang J, Nagai Y, Hasegawa M, Ohkubo T, Eldrup M, Singh BN. 3D-AP and positron annihilation study of precipitation behaviour in Cu-Cr-Zr alloy. J. Nucl. Mater. 2009;386–388:852–5.
[19] Zhang K, Gaganidze E, Gorley M. Development of the material property handbook and database of CuCrZr. Fus. Eng. Des. 2019;144:148–53.
[20] Roussel LY, Stokes DJ, Gestmann I, Darus M, Young RJ. Extreme high resolution scanning electron microscopy (XHR SEM) and beyond. In: In Proceedings of the SPIE 7378, Scanning Microscopy 2009; May 2009. 73780W.
[21] Young R, Henstra S, Chmelik J, Dingle T, Mangnus A, van Veen G, Gestmann I. XHR SEM: enabling extreme high-resolution scanning electron microscopy. In: In Proceedings of the SPIE 7378, Scanning Microscopy, Monterey, California, United States; 2009.
[22] Humphreys FJ. Grain and subgrain characterisation by electron backscatter diffraction. J. Mater. Sci. 2001;36:3833–54.
[23] Humphreys FJ. Quantitative metallography by electron backscattered diffraction. J. Microsc. 1999;195:170–85.
[24] Delille D, Pantel R, Van Cappellen E. Crystal thickness and extinction distance determination using energy filtered

{CBED} pattern intensity measurement and dynamical diffraction theory fitting. Ultramicroscopy 2001;87:5–18.
[25] Miller MK, Russell KF. Atom probe specimen preparation with a dual beam SEM/FIB miller. Ultramicrosc 2007;107:761–6.
[26] Asoka-Kumar P, Alatalo M, Ghosh VJ, Kruseman AC, Nielsen B, Lynn KG. Increased Elemental Specificity of Positron Annihilation Spectra. Phys. Rev. Lett. 1996;77:2097–100.
[27] Maeda N, Nakamura N, Uchida M, Ohta Y, Yoshida K. Application of positron annihilation line-shape analysis to fatigue damage for nuclear plant materials. Nucl. Eng. Des. 1996;167:169–74.
[28] Kirkegaard P, Olsen JV, Eldrup M, Pedersen NJ. PALSfit: a Computer Program for Analysing Positron Lifetime Spectra. 2009.
[29] Nagai Y, Hasegawa M, Tang Z, Hempel A, Yubuta K, Shimamura T, Kawazoe Y, Kawai A, Kano F. Positron confinement in ultrafine embedded particles: Quantum-dot-like state in an Fe-Cu alloy. Phys. Rev. B 2000;61:6574–8.
[30] Xiong B, Mao W, Tang X, He C. Positron annihilation characteristics in mesostructural silica films with various porosities. J. Appl. Phys. 2014;115:094303.
[31] Holzwarth U, Stamm H. The precipitation behaviour of ITER-grade Cu-Cr-Zr alloy after simulating the thermal cycle of hot isostatic pressing. J. Nucl. Mater. 2000;279:31–45.
[32] Puska MJ, Lanki P, Nieminen RM. Positron affinities for elemental metals. J. Phys.: Condens. Matter 1989;1:6081–93.
[33] Almazouzi A, Macht M-P, Naundorf V, Neumann G. Diffusion of Manganese, Chromium, and Titanium in Single Crystalline Copper. Phys. Stat. Sol. (a) 1998;167:15–28.
[34] Clement M, de Nijs JMM, Balk P, Schut H, van Veen A. Transport of positrons in the electrically biased metal-oxide-silicon system. J. Appl. Phys. 1997;81:1943–55.
[35] Bordulev I, Kudiiarov V, Svyatkin L, Syrtanov M, Stepanova E, Cízek J, et al. Positron annihilation spectroscopy study of defects in hydrogen loaded Zr-1Nb alloy. J. Alloys Comp. 2019;798:685–94.
[36] Troev T, Markovski A, Peneva S, Yoshiie T. Positron lifetime calculations of defects in chromium containing hydrogen or helium. J. Nucl. Mater. 2006;359:93–101.
[37] Ivanov AD, Nikolaev AK, Kalinin GM, Rodin ME. Effect of heat treatments on the properties of CuCrZr alloys. J. Nucl. Mater. 2002;307-311:673–6.
[38] Fu H, Xu S, Li W, Xie J, Zhao H, Pan Z. Effect of rolling and aging processes on microstructure and properties of Cu-Cr-Zr alloy. Mater. Sci. Eng A 2017;700:107–15.
[39] Chen J, Wang J, Xiao X, Wang H, Chen H, Yang B. Contribution of Zr to strength and grain refinement in Cu-Cr-Zr alloy. Mater. Sci. Eng. 2019;756:464–73.
[40] Jinshui C, Bin Y, Junfeng W, Xiangpen X, Huiming C, Hang W. Effect of different Zr contents on properties and microstructure of Cu-Cr-Zr alloys. Mater. Res. Express 2018;5:026515.
[41] Jha K, Neogy S, Kumar S, Singh RN, Dey GK. Correlation between microstructure and mechanical properties in the age-hardenable Cu-Cr-Zr alloy. J. Nucl. Mater. 2021;546:152775.
[42] Liu J, Hou M, Yang H, Xie H, Yang C, Zhang J, et al. In-situ TEM study of the dynamic interactions between dislocations and precipitates in a Cu-Cr-Zr alloy. J. Alloys Comp. 2018;765:560–8.
[43] Wang H, Gong L, Liao J, Chen H, Xie W, Yang B. Retaining meta-stable fcc-Cr phase by restraining nucleation of equilibrium bcc-Cr phase in CuCrZrTi alloys during ageing. J. Alloys Comp. 2018;749:140–5.
[44] Che X, Jiang F, Liu L, Hunag H, Shi Z. Structure and orientation relationship of new precipitates in a Cu-Cr-Zr alloy. Mater. Sci. Technol. 2018;34(3):282–8.